

Mesostructured MTES-Derived Silica Thin Film with Spherical Voids Investigated by TEM: 1. Mesostructure Determination

K. Yu,^{*,†} X. Wu,[‡] C. J. Brinker,[§] and J. Ripmeester[†]

Steeacie Institute for Molecular Sciences, National Research Council of Canada, Ottawa, Ontario K1A 0R6, Canada, Institute for Microstructural Sciences, National Research Council of Canada, Ottawa, Ontario K1A 0R6, Canada, and Sandia National Laboratories, MS 1349, Albuquerque, New Mexico 87185, and Center for Micro-Engineered Materials, University of New Mexico, Albuquerque, New Mexico 87131

Received February 21, 2003. In Final Form: May 29, 2003

The mesostructure of a hydrophobic silica thin film with spherical voids arranged in an ordered array was investigated and resolved thoroughly by transmission electron microscopy (TEM). The novel TEM approach involved sample tilting to get different zone axes and simulation, as well as the calculation of plane spacings and angles for comparison of the experimental values with the corresponding theoretical ones. The camera constant (λL) was calibrated carefully by the diffraction pattern of the silicon substrate, on which the closed-cell mesostructured thin film was developed. This film was fabricated by solvent evaporation-induced sol–gel and self-assembly processes, with methyl triethoxysilane [MTES, $\text{Si}(\text{OCH}_2\text{CH}_3)_3\text{CH}_3$] as the silica precursor and a polystyrene-*block*-poly(ethylene oxide) diblock as the structure-directing agent; pyrolysis was performed carefully to remove the template. The present TEM exploration concludes that the mesostructure is exclusively body-centered cubic (bcc) rather than face-centered cubic (fcc); this conclusion was based on the assessment of the experimental tilting angles and the theoretical angles employed to get one zone axis from another, as well as on the evaluation of the experimental and simulated TEM images. The bcc mesostructure with a slight distortion was further assigned to be body-centered tetragonal (bct) with the preferred cell parameters of $a = 13.5$ nm and $c = 13.0$ nm; this assignment was based on the comparison between the experimental and the calculated data, including the plane spacings and the angles between various planes. The present self-assembled MTES-derived silica thin film with closed cells arranged in a slightly distorted bcc array is believed to be the first and is a promising candidate to function as a low-dielectric-constant (k) insulating material needed for future semiconductor devices.

1. Introduction

A great deal of interest in the synthesis of various mesostructured porous inorganic oxides emerged in 1992,¹ since then, a large variety of surfactant-templated silica materials have been synthesized in the form of powders, particles, and thin films.^{2–4} Mesoporous materials in the form of thin films are good candidates for various applications such as hosting optically active or quantum confined species as sensors. Furthermore, it has been proposed that the introduction of pores into silica, which ideally should be nanosized voids (isolated rather than interconnected) with a uniform distribution will lead to the next generation of dielectric insulators with low dielectric constants (k).⁵ Preferential solvent evaporation-induced sol–gel and self-assembly (EISGSA) processes

at ambient temperature and pressure have brought a new perspective to the fabrication of silica/surfactant hybrid thin films with well-ordered mesostructures.⁴ However, after pyrolysis, the mesostructured pores are usually interconnected through micropores in the silica wall; in addition, the hydrophobicity of tetraethoxysilane-derived silica thin films is low.

We first reported on the use of PS-based amphiphilic diblock copolymers with a high glass transition temperature ($T_g \approx 373$ K), namely, polystyrene-*block*-poly(ethylene oxide) (PS-*b*-PEO) diblocks, to synthesize silica/amphiphile thin films with regular and reverse mesophases, as well as curved multilamellar mesostructures, through the so-called EISGSA processes.⁶ Among the usually observed mesophases there was a brand-new one consisting of an ordered arrangement of spherical microdomains that were isolated from each other.

In the fabrication of this mesophase, tetraethoxysilane [TEOS, $\text{Si}(\text{OCH}_2\text{CH}_3)_4$] and methyl triethoxysilane [MTES, $\text{Si}(\text{OCH}_2\text{CH}_3)_3\text{CH}_3$], as well as a mixture of MTES and TEOS, were used as silica precursors.⁷ The synthetic approach was designed to suppress the silicate condensation, to allow co-self-assembly (of the silicates and the

* To whom correspondence should be addressed.

[†] Steeacie Institute for Molecular Sciences, National Research Council of Canada.

[‡] Institute for Microstructural Sciences, National Research Council of Canada.

[§] Sandia National Laboratories and University of New Mexico.

(1) Kresge, C.; Leonowicz, M.; Roth, W.; Vartuli, C.; Beck, J. *Nature* **1992**, *359*, 710.

(2) (a) Huo, Q.; Margolese, D. I.; Clesla, U.; Feng, P.; Gler, T. E.; Slegler, P.; Leon, R.; Petroff, P. M.; Schuth, F.; Stucky, G. D. *Nature* **1994**, *368*, 317. (b) Tanev, P. T.; Pinnavaia, T. J. *Science* **1995**, *267*, 865. (c) Smarsly, B.; Goltner, C.; Antonietti, M.; Ruland, W.; Hoinkis, E. J. *Phys. Chem. B* **2001**, *105*, 831.

(3) (a) Antonelli, D. M.; Ying, J. Y. *Angew. Chem., Int. Ed. Engl.* **1995**, *34*, 2014. (b) Mann, S.; Ozin, G. A. *Nature* **1996**, *382*, 313. (c) Ozin, G. A.; Chomski, E.; Khushalani, D.; MacLachlan, M. J. *Curr. Opin. Colloid Interface Sci.* **1998**, *3*, 181.

(4) (a) Ogawa, M. *J. Am. Chem. Soc.* **1994**, *116*, 7941. (b) Brinker, C. J.; Lu, Y.; Sellinger, A.; Fan, H. *Adv. Mater.* **1999**, *11*, 579.

(5) Miller, R. D. *Science* **1999**, *286*, 421.

(6) Yu, K.; Hurd, A. J.; Eisenberg, A.; Brinker, C. J. *Langmuir* **2001**, *17*, 7961.

(7) (a) Yu, K.; Smarsly, B.; Brinker, C. J. *Mater. Res. Soc. Symp. Proc.* **2002**, *728*, S1.9. (b) Yu, K.; Smarsly, B.; Brinker, C. J. *Adv. Funct. Mater.* **2003**, *13* (1), 47–52. (c) Smarsly, B.; Xomeritakis, G.; Yu, K.; Liu, N.; Fan, H.; Assink, R. A.; Drewien, C. A.; Ruland, W.; Brinker, C. J. *Langmuir* **2003**, *19*, 7295–7301. (d) Smarsly, B.; Yu, K.; Brinker, C. J. *Stud. Surf. Sci. Catal.* **2003**, *146*, 295–298.

template) accompanied and followed by the careful PEO retraction from the sol-gel matrix, leaving no additional microporosity, without gas permeability due to the continuous rearrangement of the matrix and consolidation. Mesostructured silica thin films with closed cells as well as with tuneable hydrophobicity were obtained after careful pyrolysis.⁷ Various experiments, such as thermal gravimetric analysis, surface acoustic wave nitrogen adsorption, contact-angle measurements, ¹³C and ²⁹Si direct polarization magic angle spinning solid state nuclear magnetic resonance spectroscopies, and two-dimensional grazing incidence small angle X-ray scattering (GISAXS), were carried out to characterize the as-prepared and calcined thin films in detail. A solvent-mediated mechanism was proposed to account for the absence of microporosity, namely, the absence of the interconnectivity of the mesopores. The quantitative absence of additional microporosity in the matrix (after PEO removal) was demonstrated by GISAXS with a theoretical approach, the so-called chord-length distribution. For the mesostructure, the GISAXS experiment favored a body-centered cubic (bcc) lattice, without giving conclusive results between bcc and face-centered cubic (fcc) lattices because of a lack of three-dimensional information about the pore arrangement. A bcc mesostructure throughout the whole film (and not only locally), with a slight distortion and a lattice parameter of about 13.0 nm, was recommended.⁷ Nevertheless, the transmission electron microscopy (TEM) study left the structural distinction of bcc versus fcc unresolved.⁷

With respect to the self-assembly of the diblock in the fabrication process, it is also difficult to determine unambiguously whether the ordered structure is bcc or fcc in nature. It is necessary to point out that self-assembly in the present system goes through different concentration regions.⁸ Therefore, a brief description of the self-assembly of diblock copolymers in dilute, semidilute, and concentrated solutions, as well as in the bulk, is provided. Although this introduction is qualitative and highly simplified, it is of help to have an overview of the compulsory requirements for the investigation of bcc vs fcc structures in the present system. In general, spherical micelles form in a dilute solution of a selected solvent at a fixed temperature when micellization occurs.⁹ In semidilute and concentrated solutions, there is a general agreement that gelation takes place because of the population increase of spherical micelles with increasing temperature; both fcc and bcc structures have been observed, but not the simple cubic (sc) ones.¹⁰ The volume fractions (Φ) of spheres in various cubic systems are different and can reach values as high as 0.74, 0.68, or 0.49 in a fcc, bcc, or sc structure, respectively.¹¹ In the bulk, the morphologies (including bcc-organized spheres, hexagonal-arranged rods, and lamellae) of microphase-separated AB diblock copolymers are usually a function of the copolymer composition, namely, the volume ratio of the two blocks.¹² It is acknowledged that the formation mechanism of the mesostructured silica/PS-*b*-PEO thin

films is of interest;⁸ however, the present study does not address this feature, but only the mesostructural dilemma of bcc versus fcc.

In the present publication, we report on the determination of the mesostructure of the MTES-derived silica thin films with ordered voids using TEM. By this approach, the mesostructure is determined unambiguously to be slightly distorted bcc and is cautiously assigned to be a body-centered tetragonal (bct) structure with the cell parameters of $a = 13.5$ nm and $c = 13.0$ nm. The present self-assembled MTES-derived silica thin film with isolated bct-arranged voids provides a conceptual route to the fabrication of materials with nanosized voids arranged in a cubic array as well as with controllable hydrophobicity, whose k values could be extended promisingly to the ultralow k range ($k < 2.2$).⁵

2. Experimental Section

Mesostructured silica films were prepared by EISGSA; a detailed description can be found elsewhere.⁶⁻⁸ The synthesis began with a tetrahydrofuran solution containing PS(35)-*b*-PEO-(109) diblock copolymer (with 35 styrene units and 109 ethylene oxide units from Polymer Source, Inc.), MTES, and hydrogen chloride (HCl), as well as Milli-Q water; a weight ratio of about 1:7 copolymer/MTES as well as molar ratios of 1:0.004:5 MTES/HCl/H₂O were acquired. After one drop of the solution was cast onto the surface of a (001) silicon (Si) wafer (ca. 0.54 mm in thickness) and subsequent gelation, pyrolysis was carried out in argon (with a heating rate of 1 °C/min to 400 °C for 3 h) to remove the template and to produce a non-free-standing silica thin film with nanosized spherical voids arranged in an ordered array.

The mesostructure of the calcined MTES-derived silica thin film on the Si wafer was characterized by TEM. Two methods of TEM sample preparation were carried out: one was by scratching; the other was by using the cross section. The first sample was prepared by scratching the film with a pair of tweezers and directly dispersing fragments onto a holey TEM carbon-coated copper grid. For the cross-sectional sample, two bars (ca. 1 mm in width and 4 mm in length) were cut out of the wafer and glued together with the film sides face to face; the glue used was M-bond 610 transparent epoxy (Measurements Group, Inc., Raleigh, NC). Afterward, a disk (3 mm in diameter in the central part) was constructed from the glued object with an ultrasonic disk cutter (Gatan, model 601). This disk was thinned mechanically from about 1 mm to about 100 μ m in thickness. The thinned disk was dimpled from both sides with 3 μ m of diamond paste, until its central part reached approximately 20 μ m in thickness. The dimpled disk was then polished from both sides with 1 μ m of diamond paste to achieve very smooth surfaces. A final thinning to perforation was conducted using Ar ion milling (Precision Ion Polishing System, Gatan, model 691) from both sides with an ion beam angle of 8° and a gun voltage of 6 kV. The TEM samples were loaded in a double tilt sample holder and examined in a Philips EM 430T operated at 200 kV. The relativistic wavelength (λ) of the electron at a 200-kV accelerating voltage is 0.0251 Å.

3. Results and Discussion

As was mentioned before, the present self-assembled sol-gel MTES-derived silica thin film with spherical voids on a nanometer scale and organized in an ordered array is a promising candidate for low- k dielectric materials in future micro-electronic devices. In the preparation of such silica/PS-*b*-PEO hybrid thin films as well as subsequent pyrolysis, a number of factors and the interplay between them influence both the meso- and microstructures.⁶⁻⁸ In general, our synthetic design was aimed at the formation of spherical microdomains with the co-self-assembly to be accompanied by a PEO retraction from the matrix but without leaving additional microporosity. Also, the design

(8) Yu, K.; Drewien, C. A.; Hurd, A. J.; Brinker, C. J.; Eisenberg, A. *Mater. Res. Soc. Symp. Proc.* **2001**, *672*, O8.15.

(9) (a) Price, C. In *Developments in block copolymers*; Goodman, I., Ed.; Applied Science Publishers: London, 1982; Vol. 1, p 39. (b) Halperin, A.; Tirrel, M.; Lodge, T. P. *Adv. Polym. Sci.* **1992**, *100*, 31. (c) Gao, Z.; Varshney, S. K.; Wong, S.; Eisenberg, A. *Macromolecules* **1994**, *27*, 7923. (d) Yu, K.; Bartels, C.; Eisenberg, A. *Langmuir* **1999**, *15*, 7157.

(10) (a) McConnell, G. A.; Gast, A. P.; Huang, J. S.; Smith, S. D. *Phys. Rev. Lett.* **1993**, *71*, 2102. (b) Wanka, G.; Hoffmann, H.; Ulbricht, W. *Macromolecules* **1994**, *27*, 4145.

(11) (a) Hoover, W. G.; Ree, F. H. *J. Chem. Phys.* **1968**, *49*, 3609. (b) Scordari, F. Ionic Crystals. In *Fundamentals of Crystallography*; Giacovazzo, C., Ed.; Oxford University Press: Oxford, 1992; p 429.

(12) (a) Matsen, M. W.; Bates, F. S.; *Macromolecules* **1996**, *29*, 1091. (b) Bates, F. S.; Fredrickson, G. H. *Annu. Rev. Chem.* **1990**, *41*, 525.

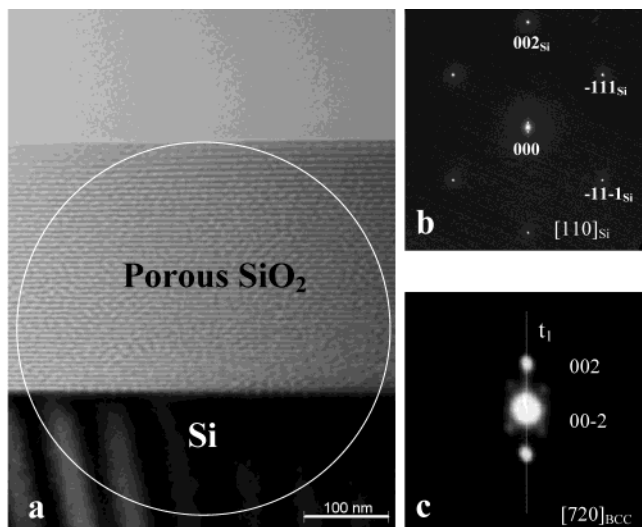


Figure 1. (a) Representative TEM image of the cross-sectional sample prepared, showing both the silica film with spherical voids arranged in a cubic array and the Si substrate. (b) Diffraction patterns of both the film and the substrate recorded at the same time with $L = 2900$ mm. The indices for Si are presented with the subscript Si; the Si zone axis is $[110]$. (c) Enlarged diffraction pattern of the film by a factor of 10, the indices are for the mesostructure being bcc $[720]$.

was endeavored to allow the template decomposition products to diffuse out through the matrix at the early stages of pyrolysis; however, the matrix became gas impermeable at the later stages of this process. Although the GISAXS experiment confirmed the quantitative absence of additional microporosity, these studies did not reach a final conclusion as to whether the ordered array of the nanosize voids is bcc or fcc in nature.^{6–8} To determine unequivocally the three-dimensional mesostructure as well as the unit-cell parameters, a novel TEM approach was developed. It involves systematic simulation of sample tilting and a comparison of the experimental data with theoretical values of the plane spacings and angles. In consequence, the Results and Discussion section consists of three parts. The study of tilting for the achievement of different zone axes of the mesostructured thin film is presented in the first part. The simulation of TEM images is addressed in the second part. The third part contains the comparison of the experimental data with theoretical values of the plane spacings and angles.

3.1. Tilting Experiments To Acquire Several Zone Axes. The cross-sectional TEM sample was studied first. Figure 1a is a representative TEM image of both the film and the substrate; this image was recorded after the sample was tilted slightly to get the Si $[110]$ zone axis. Figure 1b presents the diffraction patterns acquired from the circled area in Figure 1a, with the camera length $L = 2900$ mm; the diffraction patterns of the film and the substrate were recorded simultaneously. The Si diffraction spots in Figure 1b are indexed with the subscript Si. The central part of Figure 1b is shown in Figure 1c with an enlargement factor of 10, the diffraction pattern of which is from the film. Parts b and c of Figure 1 demonstrate that the Si $[001]$ direction [the so-called z axis that is perpendicular to the surface (001) of the wafer on which the sol-gel thin film was developed] is also a certain direction (identified as t_1 and indicated in Figure 1c) of the film. This is due to the fact that both 002 and $0,0,-2$ Si diffraction spots and two film diffraction spots are lined up along this z axis.

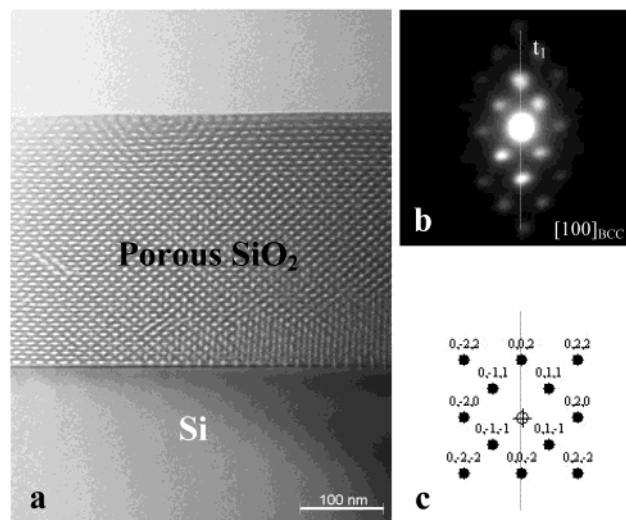


Figure 2. Cross-sectional sample tilted 16° from that in Figure 1a with t_1 as the tilting axis: (a) the TEM image, (b) the diffraction pattern, and (c) indices for bcc $[100]$.

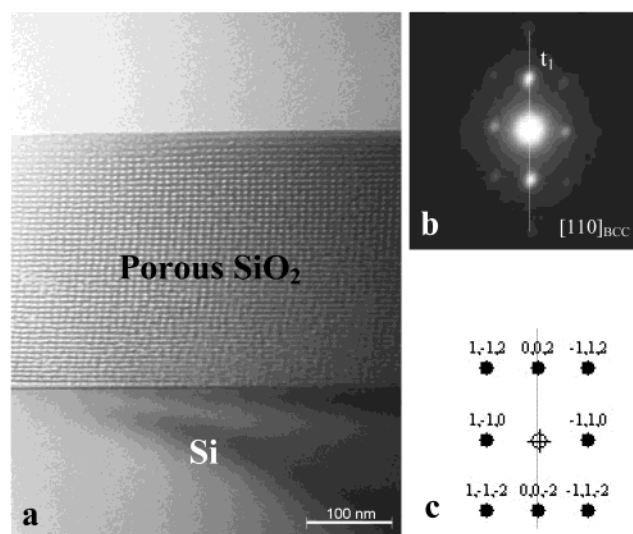


Figure 3. Cross-sectional sample tilted 29° from that in Figure 1a in an opposite direction (compared to the one from Figure 1a to Figure 2a), still with t_1 as the tilting axis: (a) the TEM image, (b) the diffraction pattern, and (c) indices for bcc $[110]$.

From now on, only the silica thin film is addressed; all the diffraction patterns were recorded with $L = 2900$ mm and the ones presented have an enlargement factor of 10. With this t_1 direction as the tilting axis, the sample was tilted 16° from the Figure 1 position, and a low-index zone axis was obtained. The TEM image is presented in Figure 2a, and the corresponding film diffraction pattern is shown in Figure 2b. For the film TEM image (Figure 2a), the regions with increased brightness compared to that of their surroundings are organized in a parallelogram-like array; they are hollow spheres rather than cylinders by nature. The sizes of these bright spots are very uniform. Moreover, from the Figure 1 position, also along this t_1 direction, the sample was tilted 29° in the opposite direction (comparing Figure 1 to Figure 2), and another low-index zone axis was obtained; the TEM image and the corresponding film diffraction pattern are presented in parts a and b of Figure 3, respectively.

It is helpful to point out that the zone axes of the film shown in Figures 1–3 should be of the $[u, v, 0]$ type, because $[001] \cdot [uvw] = 0$ gives $w = 0$. Hence, a sc structure can be

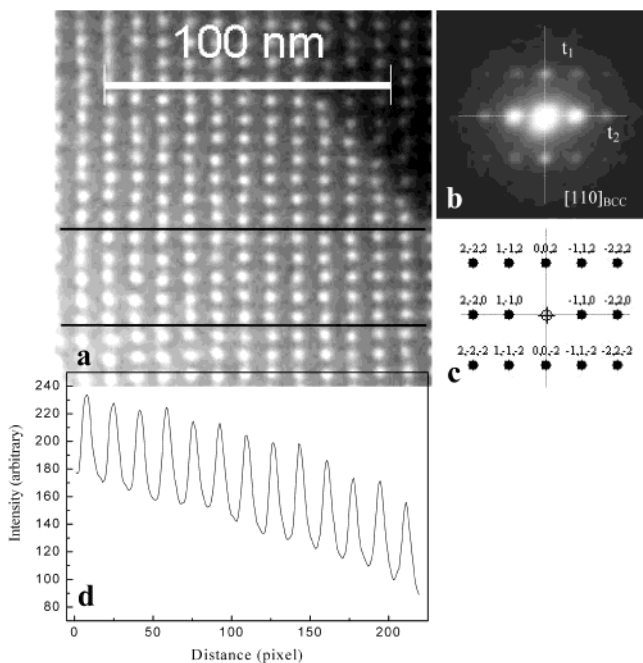


Figure 4. Scratched sample tilted to get the same zone axis shown in Figure 3: (a) a representative TEM image with two black lines providing the area used to measure d_{110} , (b) the diffraction pattern, with t_2 perpendicular to t_1 , (c) the indices for bcc $[110]$, and (d) the line profile used for the measurement of d_{110} .

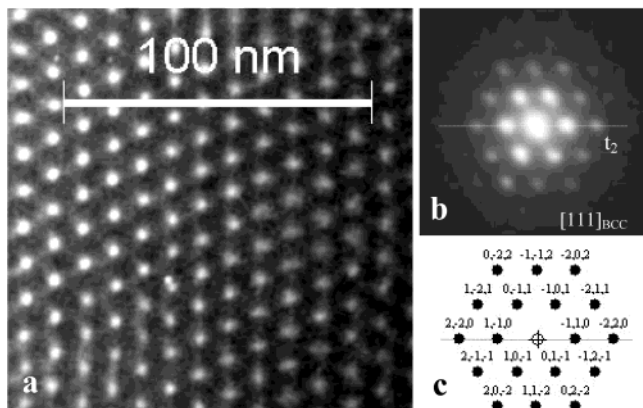


Figure 5. Scratched sample tilted 34° from the Figure 4 position with the t_2 as the tilting axis: (a) the TEM image, (b) the diffraction pattern, and (c) the indices for bcc $[111]$.

easily ruled out because of the fact that for a sc arrangement the TEM images as well as their corresponding diffraction patterns of the $[u,v,0]$ zone axes are always square or rectangular and are not the same as the ones shown in parts a and b of Figure 2, respectively.

Following the cross-sectioned sample, the scratched sample was studied, and two zone axes were obtained. This sample was tilted first to get the same zone axis as that shown in Figure 3; one TEM image and its corresponding diffraction pattern are demonstrated in parts a and b of Figure 4, respectively. From the position in Figure 4, with the t_2 direction (indicated in Figure 4b) as a tilting axis, the sample was tilted 34° to get a fourth low-index zone axis; the TEM image as well as its corresponding diffraction pattern are shown in parts a and b of Figure 5, respectively.

Subsequently, four zone axes (Figures 1–5) are obtained from the tilting experiments. According to the feature of each TEM image and its corresponding diffraction pattern

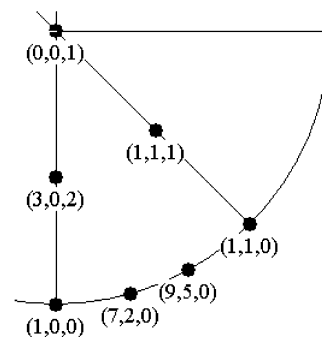


Figure 6. (001) standard stereographic projection for cubic structures, illustrating the tilting experiments in the acquisition of the different zone axes, which are represented by points and are labeled as the mesostructure being bcc or fcc.

Table 1. Experimental Tilting Angles, as Well as the Corresponding Fitted Zone Axes with Similar Angles Needed When Changing from One Zone Axis to Another, under the Assumption of bcc and fcc

figures	experimental tilting angles	zone axes of bcc and corresponding angles needed	zone axes of fcc and corresponding angles needed
1 → 2	16°	$720 \rightarrow 100, 15.95^\circ$	$950 \rightarrow 110, 15.95^\circ$
1 → 3	29°	$720 \rightarrow 110, 29.05^\circ$	$950 \rightarrow 100, 29.05^\circ$
4 → 5	34°	$110 \rightarrow 111, 35.26^\circ$	$100 \rightarrow 302, 33.69^\circ$

presented in Figures 2–5, however, the possible zone axes of Figures 2, 3, and 5 can either be bcc $[100]$, $[110]$, and $[111]$, respectively, or fcc $[110]$, $[100]$, and $[111]$, respectively. Consequently, it is still a thorny issue to differentiate the arrangement of the spherical voids in the film to be bcc or fcc based on our experimental TEM tilting results.

Accordingly, the experimental tilting angles are used to fit the theoretical angles required, when one zone axis is tilted relative to another, under the assumption that the mesostructure is bcc or fcc. Table 1 presents the experimental tilting angles from Figure 1 to 2 and 3, as well as from Figure 4 to 5. In addition, the corresponding zone axes fitted, as well as the theoretical angles between the two fitted zone axes, are summarized in Table 1 in columns 3 and 4, under the assumption of bcc and fcc mesostructures, respectively.

Table 1 illustrates that the zone axis of Figure 1c is bcc $[720]$ or fcc $[950]$, fitting with the tilting angles needed to get Figures 2 and 3. In addition, Table 1 demonstrates that the zone axis of Figure 5 is bcc $[111]$ or fcc $[302]$, to match up the experimental tilting angle of 34° used from Figure 4 to 5. As a result, it seems highly reasonable to recommend the mesostructure to be bcc rather than fcc as a result of the fact that the characteristics of the TEM image and diffraction pattern shown in Figure 5a,b are comparable with those of bcc $[111]$ and not fcc $[302]$.

In conclusion, one (001) standard stereographic projection of the cubic structures (both bcc and fcc) is demonstrated in Figure 6. The corresponding zone axes shown in Figures 1–5 are designated as points and labeled in Figure 6 to have a clear view of the relationship between the various zone axes of a bcc or fcc arrangement regarding the tilting experiment. The starting position (Figure 1c) can be either bcc $[720]$ or fcc $[950]$, and the $[100]$ and $[110]$ zone axes can be achieved when the tilting is performed along the $[001]$ direction (namely, in the x - y plane perpendicular to the z axis), with 16° in one direction and 29° in another direction. However, from the zone axis bcc $[110]$ or fcc $[100]$, the zone axis bcc $[111]$ or fcc $[302]$ should be obtained when the tilting is carried out 34° toward the z axis. Consequently, the mesostructure is resolved as bcc

because the feature of the TEM image (Figure 5a) and diffraction pattern (Figure 5b) corresponds to that of bcc [111] and not fcc [302]. Accordingly, the indices of the diffraction spots in each diffraction pattern shown in Figures 1b, 2b, 3b, 4b, and 5b are given in Figures 1c, 2c, 3c, 4c, and 5c, respectively.

3.2. Simulation of TEM Images. To further confirm our assertion that the mesostructure is bcc rather than fcc, TEM-image simulation was carried out. The software used is the so-called CaRIne Crystallography package, which addresses 14 Bravais lattices, including cubic and tetragonal systems. This simulation program, in general, offers two-dimensional projections along various zone axes of these lattices, which can be simulated as two-phase systems consisting of monodisperse spherical objects (termed atoms in the original software) distributed in matrixes with ordered arrays. In the present simulation for cubic structures, only two parameters are mandatory: one is the diameter of the spherical objects, which represents the voids in the silica thin film; the other is the lattice constant (a).

For high-resolution TEM images of conventional lattices, the image intensity of the atoms is strongly affected by the lattice periodicity; in addition, the image features are extremely sensitive to many factors, such as the specimen orientation, small changes in the sample thickness and scattering factors of the specimen, and variations in focusing, as well as the astigmatism of the objective lens. This complexity is due to the fact that the unit-cell sizes of the traditional crystals are comparable to the TEM resolution limit, which is a few angstroms; thus, the wave functions from adjoining unit cells overlap and interfere. Consequently, three groups of data are usually required for a typical high-resolution TEM image simulation: (a) crystal structure information, (b) microscope characteristics such as the acceleration voltage, spherical aberration coefficient, and spread of focus, and (c) imaging parameters such as the objective aperture diameter, specimen thickness of the imaging area, and defocus conditions. However, for the present mesostructure, its lattice constant (ca. 13 nm) is much larger than the TEM resolution limit (a few angstroms); thereby, the TEM-image intensity of the void (ca. 4 nm in diameter) is not influenced by the structural periodicity, and each void in the unit cell is imaged independently. Accordingly, simple projections of unit cells along various zone axes are suitable to simulate TEM images.

It is acknowledged that the more accurate the void size and the lattice constant entered, the more illustrative and meaningful the simulation. For the diameter of the atoms entered, namely 4.0 nm, it is an averaged value from those directly measured from the voids shown in the TEM images (Figures 1–5). It is difficult to measure unambiguously the pore size from TEM images; the diameter measured varies with the contrast of the image processed and with the under-focus value when the image is recorded. However, the present study does not address this issue.

The lattice constant of a cubic structure can be represented by

$$a = d_{hkl} \sqrt{h^2 + k^2 + l^2} \quad (1)$$

where d_{hkl} are the plane spacings between the $\{hkl\}$ planes. In general, the plane spacings can be measured directly either from TEM images or from diffraction patterns, when the structure is known as fcc, bcc, or sc. In the present study, the very plane spacing used to acquire the lattice constant is d_{002} , which is calculated from both the TEM

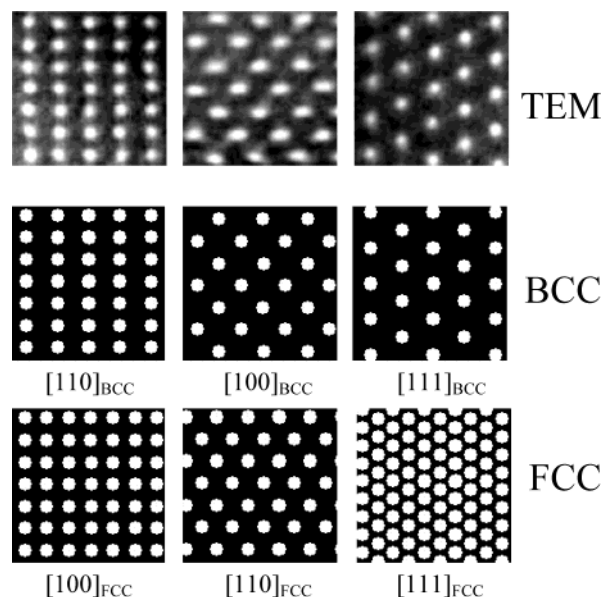


Figure 7. TEM image simulations performed for bcc and fcc structures with the lattice constant of 13.0 nm and void diameter of 4.0 nm, together with the experimental TEM images from Figures 2a, 4a, and 5a. The area of each image is the same. Each simulation is a two-dimensional projection along the zone axis indicated.

images and the diffraction patterns presented in Figures 1–4. The measurements of the plane spacing d_{hkl} are shown in detail in section 3.3.

Although the zone axis for each TEM image or diffraction pattern provided in Figures 1–5 is different when the mesostructure is assigned as bcc or fcc, the two diffraction spots, 002 and 0,0,−2, presented in the diffraction patterns of Figures 1–4 should always be indexed as 002 and 0,0,−2, respectively. This recognition is due to the fact that Figures 2 and 3 are obtained from Figure 1, via tilting along the z axis, namely the t_1 [001] direction; accordingly, the diffraction spots on this t_1 direction should always be present when other diffraction patterns are obtained. As a result, the planes perpendicular to the t_1 direction are always $\{002\}$; regarding Figures 1–4, it does not matter whether the mesophase is bcc or fcc. Figures 3 and 4 have the same zone axes. Therefore, the plane spacing d_{002} is considered only for the lattice constant in our simulation; the averaged d_{002} measured from Figures 1–4 is 6.5 nm; the lattice constant a is, thereby, 13.0 nm from eq 1.

Therefore, the parameters entered in the simulation are 4.0 nm as the diameter of the spherical objects as well as 13.0 nm as the lattice constant (a). The simulated projections of unit cells of bcc and fcc cubic structures, along the [100], [110], and [111] zone axes, are depicted in Figure 7. Because the feature of the TEM image and diffraction pattern shown in Figure 5 looks very much like cubic [111] (rather than fcc [302]), the [111] simulated images are presented in Figure 7. These simulated images illustrated are the same in size. As was pointed out before, the spherical objects represent the voids in the fabricated silica thin film; because the unit-cell dimension with the lattice constant of 13.0 nm is much larger than the TEM resolution limit (which is a few angstroms), each point (void) in the unit cell is imaged independently. Thus, the simulated images, which are the two-dimensional projections of unit cells along the different directions (as are presented in Figure 7), can be used reasonably well to compare with the experimental TEM images. For purposes of comparison, the experimental TEM images shown in Figures 2a, 4a, and 5a are also presented in Figure 7, but

Table 2. Plane Spacings (d_1 , nm) Measured from the TEM Images (d_1) and Diffraction Patterns (d_2), as Well as Calculated Values under the Assumption of bcc (d_3 , with $a = 13.0$ nm) and bct (d_4 , with $a = 13.5$ nm and $c = 13.0$ nm)

figure	planes	d_1	d_2	d_3	d_4
1a,c	002	6.5	6.4	6.5	6.5
2a,b		6.3	6.4		
3a,b		6.6	6.5		
4a,b		6.7	6.6		
2a,b	020	7.3	7.4	6.5	6.8
2a,b	011	9.3	9.4	9.2	9.4
5a,b		9.3	9.3		
3a,b	110	9.3	9.3	9.2	9.5
4a,b		9.2	9.3		
5a,b		9.6	9.7		
5a,b	101	9.1	9.2	9.2	9.4

with selected areas of the same sizes as those of the simulated ones.

Obviously, the simulated bcc images match the TEM images better than the fcc images, when the TEM images are compared with the simulated bcc and fcc ones along the three [100], [110], and [111] zone axes, as is shown in Figure 7. Consequently, the mesostructure is determined to be bcc with $a = 13.0$ nm and average diameter of the mesopores of 4 nm.

3.3. Further Investigation between bcc and bct.

Although the mesostructure was determined first as bcc, the discrepancy between the TEM and the simulated images is evident to a certain degree. To ascertain quantitatively the inconsistency, the values of the experimental plane spacings (d_{hkl}) are measured and compared with the corresponding theoretical ones. Various plane spacings (d_{hkl} , nm) are obtained and presented in Table 2; they are d_{002} from Figures 1–4, d_{020} from Figure 2, d_{011} from Figures 2 and 5, d_{110} from Figures 3–5, and d_{101} from Figure 5. These plane spacings (d_{hkl}) are acquired directly from the TEM images and from the diffraction patterns and are summarized in columns 3 and 4 as d_1 and d_2 in Table 2, respectively. In addition, theoretical values of d_{hkl} (d_3) are given correspondingly in column 5, the values of which are from a bcc structure with $a = 13.0$ nm using $d_{hkl} = a/(h^2 + k^2 + l^2)^{1/2}$.

When the plane spacing (d_{hkl}) is to be measured from the TEM image, a line profile intensity method is used for precision; image-processing software, so-called Image-Pro (Media Cybernetics, Inc.), was used. An example of this measurement is demonstrated in Figure 4d. In this line profile, the x axis gives the spatial scale (in pixels), while the y axis gives the average intensity (in an arbitrary unit); the intensity along a band from left to right between the two lines (indicated in Figure 4a) is plotted as a function of the distance (from left to right along the two lines). Each peak represents the position of a {110} plane: the thirteen peaks in Figure 4d come from the thirteen {110} planes shown in Figure 4a. Accordingly, the averaged {110} plane spacing (d_{110}) can then be calculated as

$$d_{hkl} = \frac{p_1 - p_r}{n - 1} m \quad (2)$$

where p_1 and p_r are the last and first peak positions (pixels), respectively, while n is the number of peaks and m is the magnification. In the present study, the magnification for the TEM image (Figure 4a) is 34 600. Also, negative films are scanned with the resolution of 1350 pixels/in.; thus, $m = (2.54 \times 10^7)/(1350 \times 34\ 600) = 0.5438$ nm/pixel. As is shown in Figure 4d, $p_1 = 211$ pixels, $p_r = 8$ pixels and $n = 13$. Thereby, $d_{110} = 9.2$ nm is obtained.

When the plane spacing is to be obtained from the diffraction pattern, the relationship between a certain plane { hkl } spacing (d_{hkl}) and the corresponding diffraction spot is given by

$$Rd_{hkl} = \lambda L \quad (3)$$

where R is the distance between the diffraction spot (hkl) and the transmitted (central) spot (000); when the magnification factor is not one for a presented diffraction pattern, R should be divided by the factor number. L is the camera length, and λ is the wavelength of the electrons at the given accelerating voltage when the diffraction pattern is taken. λL is a constant under one operation and is the so-called camera constant.

For accuracy, the diffraction pattern of the Si wafer (Figure 1b) was employed to calibrate the camera constant (λL) with eq 3. The Si plane spacing d_{hkl} of the plane (hkl) can be obtained from $d_{hkl} = a/(h^2 + k^2 + l^2)^{1/2}$, using the well-known Si lattice constant $a = 0.357$ nm; such Si has a diamond structure. Thus, the calibrated $(\lambda L)_c$ is 69.6 mm Å, which is close to the calculated value 72.8 mm Å, with the camera length $L = 2900$ mm and $\lambda = 0.0251$ Å. The data presented as d_2 in Table 2 are calculated with the calibrated camera constant $(\lambda L)_c$.

It is of interest to point out that the plane spacing d_{002} can also be attained from the diffraction pattern of Figure 1b. The four diffraction spots 002 and 0,0,−2 from Si and silica are considered; the simple distance ratio between Si(002) to (0,0,−2) and silica (002) to (0,0,−2) can be used to get the film d_{002} .

Because of some divergence between the d_3 values and d_i values ($i = 1-2$) in Table 2, the mesostructure should not be perfectly bcc. Therefore, a bct structure is cautiously suggested. During the EISGSA processes as well as subsequent pyrolysis, tensile stresses that are biaxial can develop in thin films coated on substrates.¹³ If a sol-gel film is not attached to any substrate, there will be no stress because of the ability to freely shrink to its stress-free state. On the other hand, if the film is non-free-standing but is constrained to a substrate, the shrinkage can only occur freely in the direction (z) perpendicular to the film/substrate interface (x - y plane). Accordingly, a bct mesophase seems to be more rational than a body-centered orthogonal one for the present slightly distorted bcc mesostructure because of the biaxial stress presented in the film. In addition, it seems logical to suggest a bct mesostructure with the lattice constant c smaller than a . Various values of a and c are considered in the comparison of bcc with bct; the plane spacing for a bct structure can be obtained from the following equation:

$$d_{hkl} = \frac{1}{\sqrt{(h^2 + k^2)/a^2 + (l/c)^2}} \quad (4)$$

Among the tested values of a and c , the bct structure with $a = 13.5$ nm and $c = 13.0$ nm seems sensible. The theoretical d_{hkl} (d_4) of this bct structure are calculated and presented correspondingly in column 6 in Table 2.

In addition to the plane spacing, the angles ϕ between various planes are also considered in the determination of the slightly distorted bcc structure. The experimental values of ϕ are compared with those calculated from the theoretical bcc and bct structures. The experimental angles ϕ between two planes are measured directly from the different patterns (shown in Figures 1–5). The measured

(13) Lu, M.; Brinker, C. J. Unpublished results. The onset of the silica condensation takes place in the very late stage of the EISA process.

results ϕ_1 are summarized in column 3 in Table 3. In addition, columns 4 and 5 in Table 3 are the correspondingly calculated angles ϕ_2 and ϕ_3 , from the bcc structure with $a = 13.0$ nm (eq 5) and the bct structure with $a = 13.5$ nm and $c = 13.0$ nm (eq 6), respectively.

$$\cos \phi = \frac{h_1 h_2 + k_1 k_2 + l_1 l_2}{\sqrt{(h_1^2 + k_1^2 + l_1^2)(h_2^2 + k_2^2 + l_2^2)}} \quad (5)$$

$$\cos \phi = \frac{(1/a^2)(h_1 h_2 + k_1 k_2) + (1/c^2)l_1 l_2}{\sqrt{[(1/a^2)(h_1^2 + k_1^2) + (1/c^2)l_1^2][(1/a^2)(h_2^2 + k_2^2) + (1/c^2)l_2^2]}} \quad (6)$$

When the calculated values from the bcc and bct structures are compared with the experimental data shown in Tables 2 and 3, there is some discrepancy. From the various combinations of a and c tested, we suggest that the mesostructure is bct with $a = 13.5$ nm and $c = 13.0$ nm. Such a suggestion is supported especially from the comparison of ϕ_2 and ϕ_3 with ϕ_1 ; the values of ϕ_3 seem to be relatively close to those of ϕ_1 compared to the values of ϕ_2 . Because of the presence of stress in the sol-gel and calcination processes, it seems almost impossible to achieve a perfect bcc mesostructure. Accordingly, the present mesostructure is not perfectly bcc (with $a = 13.0$ nm and a slight distortion) but rather bct (with $a = 13.5$ nm and $c = 13.0$ nm).

Table 3. Angles ϕ between Planes, with ϕ_1 Measured Directly from Diffraction Patterns and ϕ_2 and ϕ_3 Calculated from the bcc (with $a = 13.0$ nm) and bct (with $a = 13.5$ nm and $c = 13.0$ nm) Mesostructures, Respectively

figure	planes	ϕ_1	ϕ_2	ϕ_3
2b	002; 020	88	90	90
2b	002; 011	40	45	44
2b	011; 020	48	45	46
2b	020; 0,1,-1	50	45	46
4b	002; -1,1,0	90	90	90
5b	-1,0,1; -1,1,0	63	60	61
5b	-1,1,0; 0,1,-1	60	60	61
5b	0,-1,1; -1,0,1	58	60	59

4. Conclusions

TEM was used to characterize the mesostructure of a self-assembled hydrophobic silica thin film with spherical voids arranged in an ordered array. A TEM approach was developed to resolve the mesostructure. This method involved sample tilting to get different zone axes, simulation, and calculation. The mesostructure was conclusively found to be slightly distorted bcc rather than fcc, and probably bct. This novel self-assembled MTES-derived silica thin film should be a promising candidate for low-dielectric-constant (k) insulating materials needed for future semiconductor devices.

Acknowledgment. We thank Dr. Celeste A. Drewien for useful discussions.

Note Added after ASAP Posting. This article was released ASAP on 8/6/2003 with an error in eq 4. The correct version was posted on 8/14/2003.

LA034310H